PCCP

PAPER

View Article Online
View Journal | View Issue

Check for updates

Cite this: *Phys. Chem. Chem. Phys.*, 2022, **24**, 578

A chemical dynamics study of the reaction of the methylidyne radical (CH, $X^2\Pi$) with dimethylacetylene (CH_3CCCH_3, X^1A_{1g})†

Chao He, ‡[a] Kazuumi Fujioka,‡[a] Anatoliy A. Nikolayev, ‡[bc] Long Zhao,[a] Srinivas Doddipatla,[a] Valeriy N. Azyazov,[bc] Alexander M. Mebel, *[d] Rui Sun *[a] and Ralf I. Kaiser *[a]

The gas-phase reaction of the methylidyne (CH; $X^2\Pi$) radical with dimethylacetylene (CH_3CCCH_3; X^1A_{1g}) was studied at a collision energy of 20.6 kJ mol^{-1} under single collision conditions with experimental results merged with *ab initio* calculations of the potential energy surface (PES) and *ab initio* molecule dynamics (AIMD) simulations. The crossed molecular beam experiment reveals that the reaction proceeds barrierless *via* indirect scattering dynamics through long-lived C_5H_7 reaction intermediate(s) ultimately dissociating to C_5H_6 isomers along with atomic hydrogen with atomic hydrogen predominantly released from the methyl groups as verified by replacing the methylidyne with the D1-methylidyne reactant. AIMD simulations reveal that the reaction dynamics are statistical leading predominantly to **p28** (1-methyl-3-methylenecyclopropene, 13%) and **p8** (1-penten-3-yne, 81%) plus atomic hydrogen with a significant amount of available energy being channeled into the internal excitation of the polyatomic reaction products. The dynamics are controlled by addition to the carbon–carbon triple bond with the reaction intermediates eventually eliminating a hydrogen atom from the methyl groups of the dimethylacetylene reactant forming 1-methyl-3-methylenecyclopropene (**p28**). The dominating pathways reveal an unexpected insertion of methylidyne into one of the six carbon–hydrogen single bonds of the methyl groups of dimethylacetylene leading to the acyclic intermediate, which then decomposes to 1-penten-3-yne (**p8**). Therefore, the methyl groups of dimethylacetylene effectively 'screen' the carbon–carbon triple bond from being attacked by addition thus directing the dynamics to an insertion process as seen exclusively in the reaction of methylidyne with ethane (C_2H_6) forming propylene ($CH_3C_2H_3$). Therefore, driven by the screening of the triple bond, one propynyl moiety (CH_3CC) acts in four out of five trajectories as a spectator thus driving an unexpected, but dominating chemistry in analogy to the methylidyne – ethane system.

Received 27th September 2021,
Accepted 5th December 2021

DOI: 10.1039/d1cp04443e

rsc.li/pccp

1. Introduction

The methylidyne radical (CH, $X^2\Pi$) represents the simplest organic radical and has received considerable attention from the combustion science,[1–14] astrochemistry,[15–21] and planetary science communities[13,22–27] as a highly reactive, fundamental C1 molecular growth species. Since the very first detection of the methylidyne radical in the interstellar medium (ISM) in 1937, methylidyne has been dubbed 'ubiquitous' in deep space and has been observed toward diffuse clouds namely ζ Per,[15] molecular clouds like TMC-1,[28,29] and star forming regions such as SgrB2.[30–33] In hydrocarbon-rich atmospheres of planets and their moons such as Saturn's moon Titan, the methylidyne radical can be formed through Lyman-α (121.567 nm) photolysis of atmospheric methane[34] and has been suggested as a critical C1-building block to extend the carbon skeleton in saturated and unsaturated hydrocarbons by one carbon atom at a time.[35–42] Methylidyne can be further photo dissociated to ground state atomic carbon.[43] The importance of methylidyne radicals as a critical molecular building block is also reflected in a wealth of kinetics examinations at elevated temperatures up to 700 K[44–50] *via* room temperature studies[51–53] down to temperatures as low as 23 K[54,55] exploiting the CRESU (Kinetics of Reactions in Uniform Supersonic Flows) technique; these studies exposed barrierless reactions with hydrocarbons with

---

[a] *Department of Chemistry, University of Hawai'i at Manoa, Honolulu, Hawaii 96822, USA. E-mail: ralfk@hawaii.edu, ruisun@hawaii.edu*
[b] *Lebedev Physical Institute, Samara 443011, Russia*
[c] *Samara National Research University, Samara 443086, Russia*
[d] *Department of Chemistry and Biochemistry, Florida International University, Miami, Florida 33199, USA. E-mail: mebela@fiu.edu*

† Electronic supplementary information (ESI) available. See DOI: 10.1039/d1cp04443e

‡ Contributed equally to this work.

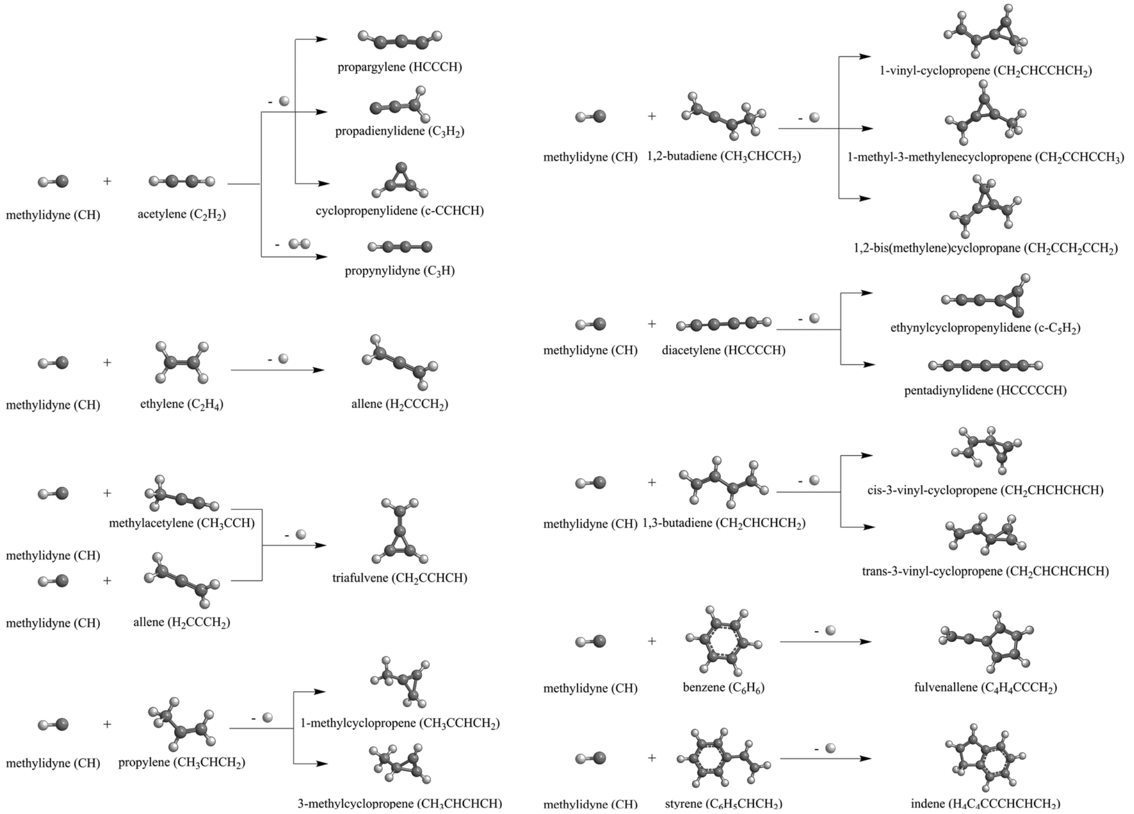

Scheme 1 Dominant products formed in the crossed molecular beam reactions of methylidyne (CH, $X^2\Pi$) radicals with unsaturated C2–C8 hydrocarbons.

rate constants of a few 10^{-10} cm^3 s^{-1}. These kinetics investigations, which predominantly are short of the identification of the 'heavy' hydrocarbon product, called for a systematic exploration of the actual reaction products under single collision conditions exploiting crossed molecular beams.[56–69] Crossed molecular beam studies of methylidyne (CH, $X^2\Pi$) and D1-methylidyne (CD, $X^2\Pi$) reactions with unsaturated C2–C8 hydrocarbons revealed a rich organic chemistry on the molecular level leading *via* atomic and also molecular hydrogen loss channels to the build-up of hydrocarbons by one carbon atom (Scheme 1).[70–79] The barrierless reactions are initiated through addition of the methylidyne radical to the π-electron density of the hydrocarbon reactant followed by isomerization through ring closure, ring opening, and hydrogen migration prior to unimolecular decomposition of the doublet radical intermediates highlighted by the formation of, *e.g.*, the cyclic hydrocarbons cyclopropenylidene (c-C_3H_2, X^1A_1),[77,78] vinylcyclopropenes (C_5H_6, X^1A'),[70,71] methylcyclopropene (C_4H_8, X^1A'),[72] triafulvene (C_4H_4, X^1A_1),[76] fulvenallene (C_7H_6, X^1A_1),[73] and indene (C_9H_8, X^1A')[75] along with the exotic carbenes triplet pentadiynylidene (C_5H_2, $X^3\Sigma_g^-$) and singlet ethynylcyclopropenylidene (c-C_5H_2, X^1A')[74] in overall exoergic reactions.

Here, we expand our crossed molecular beam studies of elementary reactions of methylidyne radicals and explore the chemical dynamic of the methylidyne (CH, $X^2\Pi$) – dimethylacetylene (CH_3CCCH_3; X^1A_{1g}) system. These experiments are combined with electronic structure calculations and *ab initio* molecule dynamics (AIMD) simulations to expose the unexpected reaction dynamics leading predominantly to 1-penten-3-yne (**p8**) (81%) and 1-methyl-3-methylenecyclopropene (**p28**) (13%) products under single collision conditions initiated by insertion of methylidyne into a carbon–hydrogen single bond and addition of the methylidyne radical to the carbon–carbon triple bond, respectively. This behavior was quite distinguishing with the related reactions of methylidyne (CH; $X^2\Pi$) radical with methylacetylene (CH_3CCH, X^1A_1)/allene (H_2CCCH_2, X^1A_1), propylene (CH_3CHCH_2; X^1A'), 1,3-butadiene ($CH_2CHCHCH_2$; X^1A_g), and 1,2-butadiene (CH_2CCHCH_3; X^1A');[70–72,76] the latter reactions carry similar reaction mechanism, which reveal non-RRKM behavior and are initiated dominantly through the barrierless addition of the methylidyne radical to the carbon–carbon double bonds and/or carbon–carbon triple bonds of the unsaturated carbon hydrogen reactants and eventually yield atomic hydrogen elimination products. By contrast, the interesting and surprising point of the current research on the reaction of methylidyne (CH, $X^2\Pi$) radical with dimethylacetylene (CH_3CCCH_3, X^1A_{1g}) suggests the most active reaction pathway is the insertion of the CH radical to one of the six C–H bonds other than the addition to the triple bond of dimethylacetylene. The main product **p8** (1-penten-3-yne) is statistically formed and is internally excited under our experimental conditions.

2. Method

2.1. Experimental

The reaction of the (D1-)methylidyne (CH/CD; $X^2\Pi$) radical with dimethylacetylene (CH_3CCCH_3; X^1A_{1g}) was studied under single collision conditions in a crossed molecular beam machine at the University of Hawaii.[22] The pulsed methylidyne molecular beam was carried out *via* photodissociation (COMPex 110, Coherent, Inc.; 248 nm; 30 Hz) of (D1)-bromoform ($CHBr_3$/$CDBr_3$, Aldrich Chemistry, ≥99%) seeded at a level of 0.1% in helium (99.9999%; AirGas) with a backing pressure of 2.2 atm.[73,76] The methylidyne radical beam passed a skimmer and was velocity selected by a four-slot chopper wheel holding a peak velocity v_p of 1826 ± 20 m s^{-1} and speed ratio S of 13.0 ± 1.4. The rotational temperature of the methylidyne beams were confirmed to be 14 ± 1 K through the technology of laser induced fluorescence (LIF).[72] The methylidyne beam collides perpendicularly with a supersonic beam of dimethylacetylene at a collision energy E_C of 20.6 ± 0.3 kJ mol^{-1} and a center of mass (CM) angle Θ_{CM} of 60.5 ± 0.7° (Table 1). The pulsed dimethylacetylene reactant was formed in the secondary source chamber with v_p of 776 ± 15 m s^{-1} and S of 9.6 ± 0.5. Each supersonic reactant beam was generated *via* a piezoelectric pulse valve, which was operated at a repetition rate of 60 Hz, a pulse width of 80 μs, and a peak voltage of −400 V. Considering the natural isotope abundance of carbon (^{12}C, 98.9%; ^{13}C 1.1%) and the potential presence of the molecular (H_2) and atomic (H) hydrogen emission channels, reactive scattering signal for the bimolecular reaction of the methylidyne radical (CH; $X^2\Pi$) with dimethylacetylene (CH_3CCCH_3; X^1A_{1g}) was probed at mass-to-charge ratios (*m*/*z*) of 67, 66, and 65. For the CD–CH_3CCCH_3 system, the reaction was conducted at a collision energy of E_C = 21.7 ± 0.4 kJ mol^{-1} and a center of mass (CM) angle of Θ_{CM} of 58.8 ± 0.5° (Table 1).

The detector comprises a Brink-type ionizer,[80] a quadrupole mass spectrometer (QMS), and a Daly-type ion counter[81] housed within a triply differentially pumped chamber rotatable in the plane defined by both supersonic reactant beams. The neutral reaction products entering the detector are ionized *via* electron impact ionization (80 eV, 2 mA),[80] then filtered according to their mass-to-charge ratios (*m*/*z*) through a QMS (Extrel; QC 150) operated with a 2.1 MHz oscillator, and ultimately detected by a Daly-type ion counter.[81] Time-of-flight (TOF) spectra were recorded at laboratory (LAB) angles in the range of $0° \leq \Theta \leq 69°$ with respect to the methylidyne radical beam (Θ = 0°). A forward-convolution routine was used to fit the laboratory data; this procedure represents an iterative method exploiting a user-defined center-of-mass (CM) translational energy $P(E_T)$ and angular $T(\theta)$ flux distributions. These functions are varied iteratively until best fits of the TOF data and angular distribution are achieved.[82,83] These functions define the reactive differential cross section $I(u, \theta) \sim P(u) \times T(\theta)$ with the center-of-mass velocity u.[84–88] The error ranges of the $P(E_T)$ and $T(\theta)$ functions are determined within 1σ limits of the errors in the corresponding laboratory angular distribution, velocity spreads, and beam velocities, while maintaining a good fit of the laboratory TOF spectra.

Table 1 Peak velocities (v_p) and speed ratios (S) of the methylidyne (CH), D1-methylidyne (CD), and dimethylacetylene (CH_3CCCH_3), along with the corresponding collision energies (E_C) and center-of-mass angles (Θ_{CM}) for the reactive scattering experiments

Beam	v_p (m s^{-1})	S	E_C (kJ mol^{-1})	Θ_{CM} (degree)
CH ($X^2\Pi$)	1826 ± 20	13.0 ± 1.4	20.6 ± 0.3	60.5 ± 0.7
CD ($X^2\Pi$)	1817 ± 14	13.0 ± 0.8	21.7 ± 0.4	58.8 ± 0.5
CH_3CCCH_3 (X^1A_{1g})	776 ± 15	9.6 ± 0.5		

2.2. Electronic structure calculations

The long-range corrected hybrid density functional ωB97X-D[89] with the 6-311G(d,p) basis set was used for geometry optimization of different species on the C_5H_7 potential energy surface (PES) accessed by the methylidyne plus dimethylacetylene reaction, including the reactants, products, intermediates, and transition states. The same ωB97X-D/6-311G(d,p) level of theory was then employed to compute vibrational frequencies for each stationary structure. The frequencies were utilized in the evaluation of zero-point vibrational energy corrections (ZPE) and in the calculations of rate constants. In order to obtain chemically accurate relative energies of various species on the C_5H_7 PES, the explicitly correlated coupled clusters method with single and double excitations and with perturbative treatment of triple excitations CCSD(T)-F12[90,91] in conjunction with Dunning's correlation-consistent cc-pVTZ-f12 basis set[92] was used to refine single-point energies of all optimized structures. The final CCSD(T)-F12/cc-pVTZ-f12//ωB97X-D/6-311G(d,p) + ZPE(ωB97X-D/6-311G(d,p)) relative energies are anticipated to be accurate within 4 kJ mol^{-1} or even better.[93] The GAUSSIAN 09[94] and MOLPRO 2010[95] quantum chemistry software codes were used for the *ab initio* calculations.

The Rice–Ramsperger–Kassel–Marcus (RRKM) approach[96–98] utilizing the energetic and molecular parameters from the electronic structure calculations was employed to evaluate energy-dependent rate constants for all unimolecular reaction steps taking place on the C_5H_7 PES following the initial bimolecular association stage. In the calculations of the energy-dependent rate constants, the internal energy for each C_5H_7 intermediate or transition state was assumed to be equal to the sum of the collision and chemical activation energies, where the chemical activation energy is a negative of the relative energy of the species relative to the separated methylidyne plus dimethylacetylene reactants. The rate constants calculations were performed using our in-house Unimol code at the zero-pressure limit,[99] with the aim to reproduce the crossed molecular beams conditions, which in turn emulate those in the outer space. The RRKM-computed rate constants were used to assess the reaction product branching ratios within the framework of steady-state approximation.[99,100]

2.3. Molecular dynamics simulations

Since *ab initio* molecule dynamics (AIMD) simulations demand millions of energy gradients, an accurate yet computationally efficient quantum chemistry method is essential to its success.

Therefore, the potential energy profile of CCSD(T)-F12/cc-pVTZ-f12//ωB97X-D/6-311G(d,p) is employed as the benchmark to evaluate the performance of a series of affordable methods such as MP2[101] and DFTs[102–107] combined with a commonly used triple-zeta basis set, 6-311(d,p).[108] Table S1 in the ESI† lists the potential energy profile of this reaction calculated from various candidate methods. The root mean square deviation (RMSD) between the benchmark and the potential energies (Table S2, ESI†) from a candidate methods is computed with eqn (1)

$$\mathrm{RMSD} = \sqrt{\frac{1}{N}\sum_{i=1}^{N}\delta_i^2}, \quad \delta_i = \mathrm{PE}(i) - \mathrm{PE}_{\mathrm{ref}}(i) \qquad (1)$$

in which δ_i is the difference in relative potential energy (with respect to the reactants) between the benchmark value ($\mathrm{PE}_{\mathrm{ref}}$) and the value calculated from the candidate method (PE) and N is the total number of key structures on the potential energy surface including the reactants, intermediates, transition states, and products. Two characteristics of a candidate method are desirable for AIMD simulations: the first is that the candidate method should accurately reproduce the benchmark potential energy surface of the reaction with small RMSD while locating all key structures, and the second is that the candidate method should render stable AIMD simulations with a reasonable time step. According to Table S2 (ESI†), the M06-2x functionals has the lowest RMSD among all tested methods, however, trial AIMD trajectories of M06-2x/6-311(d,p) display unphysical behaviors such as energy jumps between steps after getting stuck at intermediate geometries. B3LYP/6-311(d,p) level of theory is selected for its optimal balance of accuracy, speed, and stability for AIMD simulations. This protocol of selecting a quantum chemistry method for AIMD simulations studying the dynamics of chemical reactions has been widely adopted and seen great success,[109–111] including a similar chemical system of CH + C_4H_2.[74] We also note that the current study is a rare case of application of triple-zeta basis sets employed for dynamics study of a chemical reaction.

The AIMD simulations are set to model the conditions of the crossed molecular beams experiment. The reactant molecules, dimethylacetylene (C_4H_6) and the methylidyne radical (CH), are initially separated by 10 Å, sufficiently far enough that the interaction between them is negligible. The relative orientation between these two molecules is randomly sampled. The reactants are set to collide with a fixed relative translational energy of 20.6 kJ mol^{-1}. The initial vibrational and rotational energies for dimethylacetylene (C_4H_6) are selected from a canonical ensemble at 10 K, respectively, while the methylidyne radical (CH) is set to be at its ground state. This setting has been shown to accurately model bimolecular collisions of similar conditions. The positions of atoms are propagated by VENUS[112,113] (a chemical dynamics software) using the velocity Verlet algorithm with energy gradients calculated with B3LYP/6-311G(d,p) in NWChem[114,115] (a quantum chemistry software). Most of the AIMD trajectories use a 0.2 fs time step and the conservation of the physical properties such as total energy of the system is rigorously verified. The time step is decreased to as low as 0.05 fs for some unstable trajectories, which are defined as either having energy jumps between adjacent steps greater than 4 kJ mol^{-1} or energy drift over the entire trajectory greater than 8 kJ mol^{-1} with a normal (0.2 fs) time step. The trajectories are halted once either reactants (non-reactive collision) or products (reactive collision) are formed. The trajectories are also halted once they have exceeded 8 ps. In order to accurately capture the dynamics of the experiment, the AIMD simulations need to sample a large enough number of trajectories to represent the physical ensemble of the crossed molecular beam experiment. For each collision energy, the largest impact parameter, $b_{\max}$, is calculated by systematically increasing the impact parameter b. Starting from b = 0.0 Å with an increment of Δb = 1.0 Å, 40 trajectories are sampled at each impact parameter. $b_{\max}$ is identified as the largest b where at least one of the 40 trajectories is reactive. Further sampling of $b > b_{\max}$ is deemed as unnecessary for extreme low reaction probability. Since the trajectories are sampled at discrete b values, the number of trajectories at each impact parameter, $N(b)$, needs to be proportional to its area defined by the ring, $2\pi b\Delta b$. 40 trajectories are sampled at the smallest impact parameter of $b_{\min}$ = 1.0 Å and $N(b)$ is computed as in eqn (2).

$$N(b) = N(b_{\min}) \cdot \frac{b}{b_{\min}}; \quad b \leq b_{\max} \qquad (2)$$

3. Results and discussion

3.1. Laboratory system

After scaling, the TOFs are superimposable suggesting that signal at m/z = 67, 66, and 65 originates from the same reaction channel, namely the formation of C_5H_6 isomers along with atomic hydrogen (reaction (R1)). Signal at m/z = 65 ($C_5H_5^+$) is the result of dissociative electron impact ionization of the m/z = 66 ($C_5H_6^+$) parent product(s), whereas ion counts at m/z = 67 ($^{13}CC_4H_6^+$) arose from the natural abundance of carbon atom isotopes yielding $^{13}CC_4H_6$ with signal collected at a level of 3 ± 1%. Since the ion counts of the parent ion m/z = 66 ($C_5H_6^+$) were accumulated only at a level of 38 ± 4% compared to the fragment ion at m/z = 65 ($C_5H_5^+$), the TOF spectra and the laboratory angular distributions were extracted at the best signal-to-noise ratio at m/z = 65 ($C_5H_5^+$). The laboratory angular distribution is nearly symmetric around the center-of-mass angle Θ_{CM} of 60.5° and spans the angular range from 40.25° to 67.75° in the laboratory frame (Fig. 1). These findings suggest that the CH–CH_3CCCH_3 reaction proceeds *via* indirect scattering dynamics through C_5H_7 reaction intermediate(s) ultimately dissociating to C_5H_6 *via* hydrogen atom loss.

Considering hydrogen atom can be emitted from the methylidyne and/or from the six chemically equivalent hydrogen atoms of the dimethylacetylene reactant, we also explored for the reaction of D1-methylidyne (CD) with dimethylacetylene to extract detailed information on the hydrogen atom loss position(s). For the CD-dimethylacetylene system, TOFs were recorded at m/z = 67 ($C_5DH_5^+$) (reaction (R2)) and 66

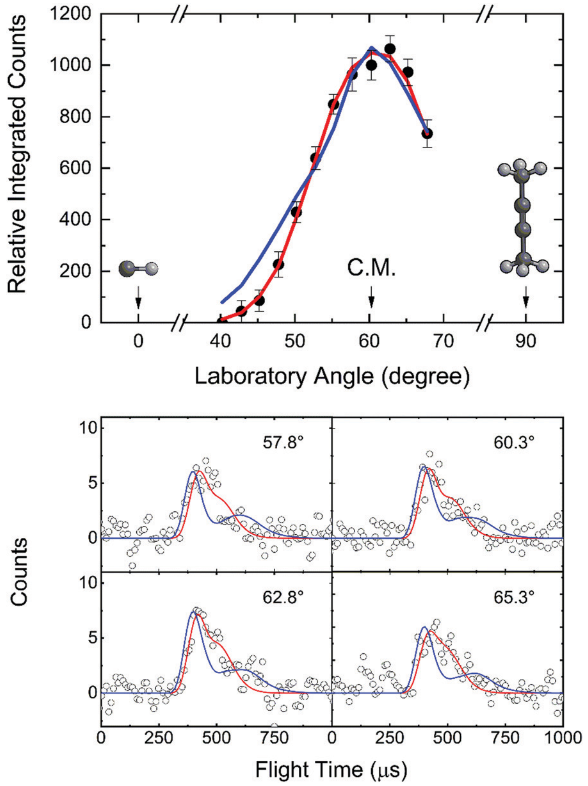

Fig. 1 Laboratory angular distribution (top) and time-of-flight (TOF) spectra (bottom) recorded at mass-to-charge (m/z) 65 ($C_5H_5^+$) from the reaction of the methylidyne radical (CH; $C_{\infty v}$; $X^2\Pi$) with dimethylacetylene (CH_3CCCH_3; D_{3d}; X^1A_{1g}). The directions of the methylidyne radical and dimethylacetylene beams are defined as 0° and 90°, respectively. The red and blue solid lines represent the best-fits exploiting center-of-mass functions depicted in Fig. 2 from the experimentally derived (red) and from the dynamics simulations (blue) with black circles defining the experimental data.

($C_5DH_4^+/C_5H_6^+$) (reaction (R3)) at a center-of-mass angle of 58.8° (Fig. S1, ESI†). Ion counts at m/z = 66 may also arise from dissociative electron impact ionization of C_5DH_5 if formed. Signal was observed both at m/z = 67 and 66 (Fig. S1, ESI†). Accounting for the ^{13}C isotopic contribution of 5.5% for five carbon atoms, the ratio of the ion counts at m/z = 67 *versus* 66 is determined to be 35 ± 3%. This ratio matches the ratio of m/z = 66 to m/z = 65 in the CH–dimethylacetylene system. These findings reveal that for the CD–dimethylacetylene reaction, ion counts at m/z = 66 can be attributed to a dissociative electron impact ionization of m/z = 67 ($C_5DH_5^+$) product(s) in the electron impact ionizer, whereas the C_5DH_5 product(s) was (were) formed *via* hydrogen atom loss from the dimethylacetylene reactant. Therefore, we may conclude that, in the reaction of the methylidyne radical (CH; 13 amu) with dimethylacetylene (CH_3CCCH_3, 54 amu), the H loss originates at least from the dimethylacetylene reactant.

$$\text{CH (13 amu)} + CH_3CCCH_3 \text{ (54 amu)} \rightarrow C_5H_6 \text{ (66 amu)} + \text{H (1 amu)} \qquad \text{(R1)}$$

$$\text{CD (14 amu)} + CH_3CCCH_3 \text{ (54 amu)} \rightarrow C_5DH_5 \text{ (67 amu)} + \text{H (1 amu)} \qquad \text{(R2)}$$

$$\text{CD (14 amu)} + CH_3CCCH_3 \text{ (54 amu)} \rightarrow C_5H_6 \text{ (66 amu)} + \text{D (2 amu)} \qquad \text{(R3)}$$

3.2. Center-of-mass system

For the methylidyne radical (CH; $X^2\Pi$) – dimethylacetylene (CH_3CCCH_3; X^1A_{1g}) reaction, the TOF spectra and LAD (Fig. 1) can be fit with a single reaction channel CH (13 amu) + C_4H_6 (54 amu) → C_5H_6 (66 amu) + H (1 amu). The best-fit CM functions are shown in Fig. 2 with the hatched areas of the $P(E_T)$ and $T(\theta)$ representing 1σ error limits. Considering the principle of conservation of energy, the maximum energy E_{max} of the CM translational energy distribution $P(E_T)$ (Fig. 2), the collision energy (E_C), and the reaction energy (Δ_rG) are linked *via* $E_{max} = E_C - \Delta_rG$ for those molecules born without internal excitation. The maximum $P(E_T)$ was derived to be 77 ± 19 kJ mol^{-1} suggests a reaction energy of −56 ± 19 kJ mol^{-1} to form C_5H_6 isomers plus atomic hydrogen. The distribution maximum of $P(E_T)$ at 12 ± 3 kJ mol^{-1} hints to a rather loose exit transition state resulting to C_5H_6 molecules formation.[116] An average translational energy of the products calculated to be 21 ± 5 kJ mol^{-1} reveals that only 27 ± 6% of the total

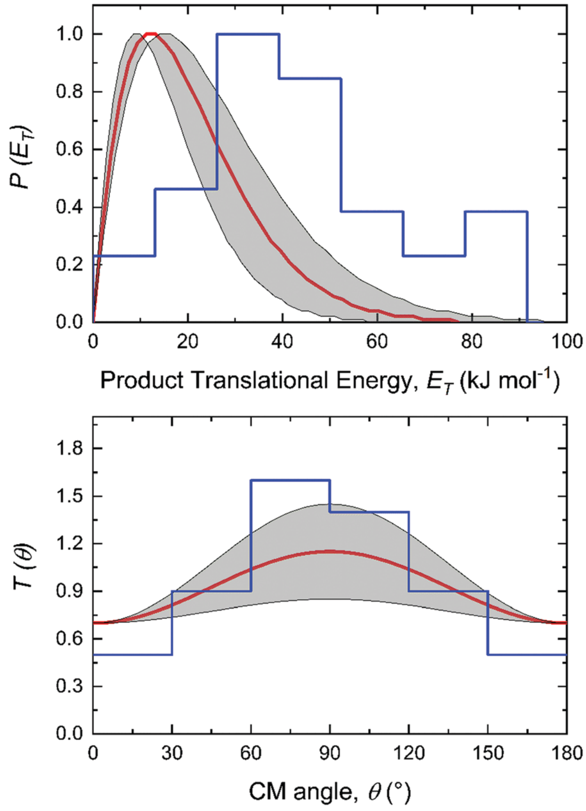

Fig. 2 Center-of-mass (CM) translational energy $P(E_T)$ and angular $T(\theta)$ flux distributions for the reaction of the methylidyne radical (CH; $C_{\infty v}$; $X^2\Pi$) with dimethylacetylene (CH_3CCCH_3; D_{3d}; X^1A_{1g}). Shaded areas indicate the error limits of the best fits accounting for the uncertainties of the laboratory angular distribution and TOF spectra, with the red solid lines defining the best-fit functions. The center-of-mass function overlaid in blue are obtained from the dynamics simulations.

available energy is channeled into the product translation degrees of freedom. These findings suggest indirect reactive scattering dynamics leading to C_5H_6 isomer(s) *via* C_5H_7 intermediate(s).[88,117] Additional information on the reaction dynamics can be obtained by examining the CM angular distribution $T(\theta)$. The $T(\theta)$ displays non-zero intensity over the complete angular range from 0° to 180° as well as forward–backward symmetric with a maximum at 90° (sideways scattering). This forward–backward symmetry implies that the lifetime of the C_5H_7 intermediate is longer than its rotational period(s).[118] The sideways scattering suggests significant geometrical constraints in the exit transition state with the hydrogen atom eliminated nearly perpendicular to the rotational plane of the decomposing intermediate and hence almost parallel to the total angular momentum vector.[84,119]

3.3. Potential energy surfaces

It is always beneficial to merge the experimental data with electronic structure and statistical calculations to propose the underlying reaction mechanism(s) leading to C_5H_6 formation (Fig. 3–8, Table 2 and Fig. S2–S5, Tables S3 and S4, ESI†). The C_5H_7 PES has been adapted from the methylidyne – 1,3-butadiene[71] and methylidyne – 1,2-butadiene reactions systems[70] and expanded to be linked to the reaction intermediates and distinct products of the reaction of methylidyne with dimethylacetylene. Overall, the methylidyne radical (CH) can add to the C≡C bond and/or insert into one of C–H bonds of dimethylacetylene involving 35 distinct C_5H_7 intermediates (**i3–i6**, **i8**, **i15**, **i31**, **i32**, **i36**, **i45**, **i49**, **i60**, **i66**, **i68**, **i70**, **i71**, **i80–i97**) and 91 transition states yielding hydrogen atom loss product (C_5H_6; **p1–p3**, **p8**, **p10**, **p12**, **p27**, **p28**, **p40**, **p41**, **p41′**), methyl (CH_3) emission products (C_4H_4; **p23**, **p39**), vinyl (C_2H_3) group loss product (C_3H_4; **p38**), and propargyl (C_3H_3) emission products (C_2H_4; **p24**, **p42**) (Fig. 3–7). Note that, because of the background counts of CH_3^+, $C_2H_3^+$, $C_2H_4^+$, $C_3H_3^+$, $C_3H_4^+$, $C_4H_4^+$ species originated from dissociative electron impact ionization of the dimethylacetylene reactant, $C_4H_4/C_3H_4/C_2H_4$ products formed *via* $CH_3/C_2H_3/C_3H_3$ losses cannot be probed under our experimental conditions. Therefore, pathways related to the atomic hydrogen loss products are discussed here.

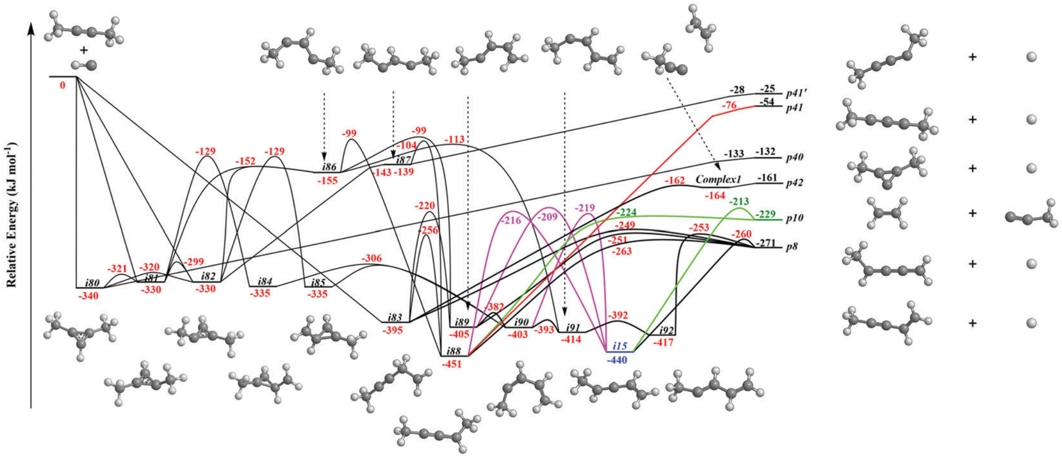

Fig. 3 Sections of the C_5H_7 potential energy surface (PES) leading to **p8**, **p10**, **p40**, **p41**, **p41′**, and **p42**.

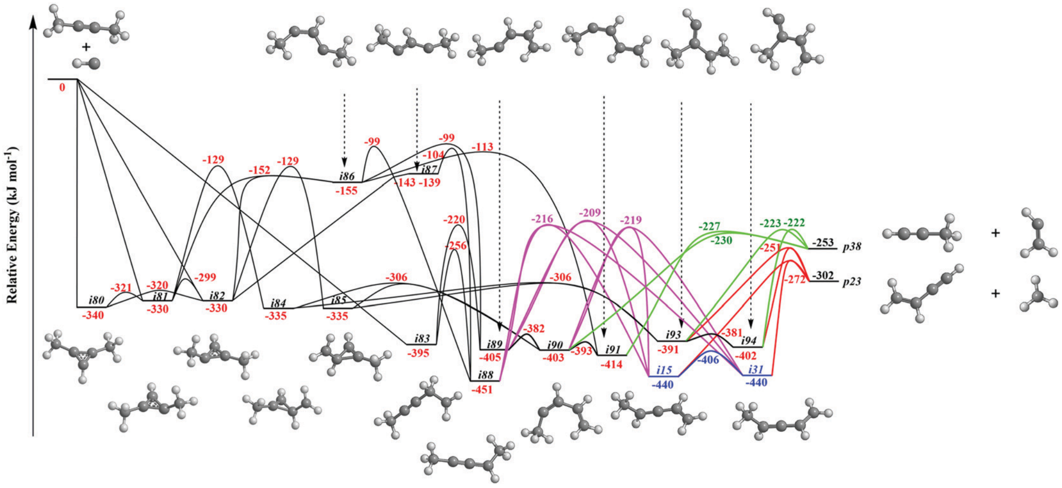

Fig. 4 Sections of the C_5H_7 PES leading to **p23** and **p38**.

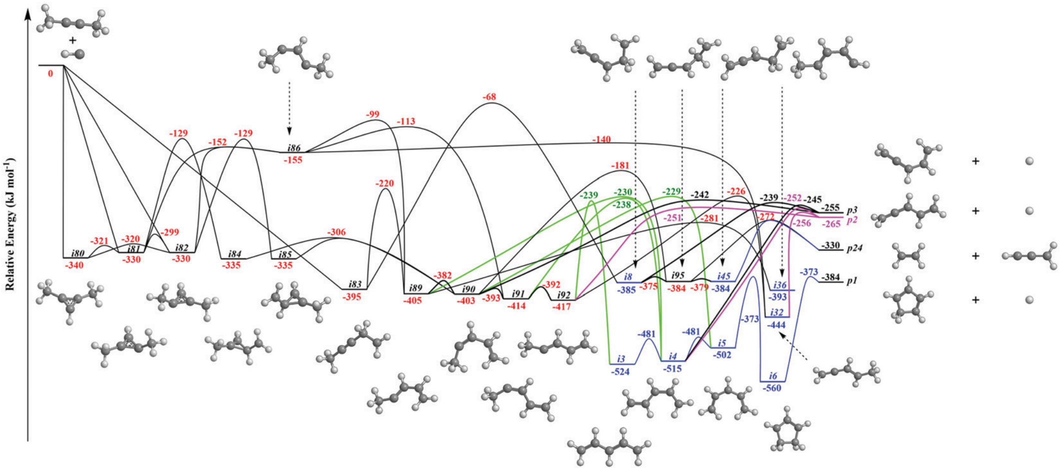

Fig. 5 Sections of the C_5H_7 PES leading to **p1–p3**, and **p24**.

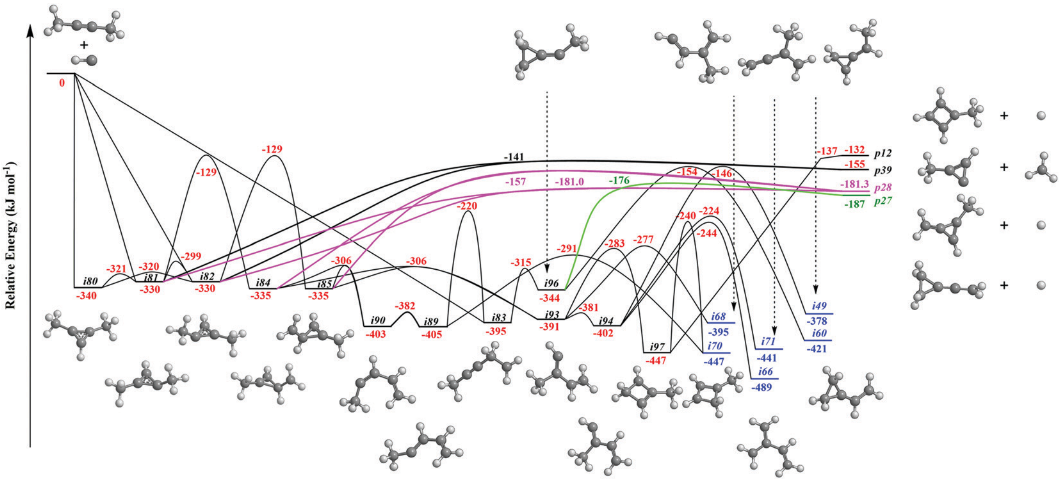

Fig. 6 Sections of the C_5H_7 PES leading to **p12**, **p27**, **p28**, and **p39**.

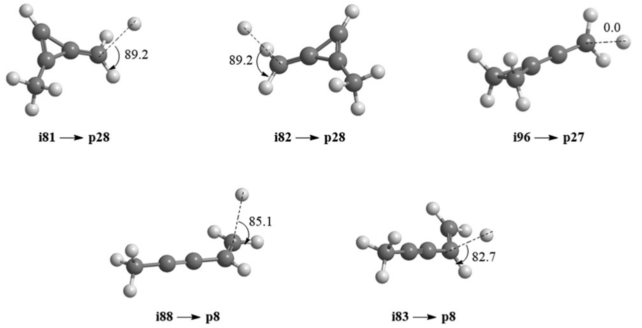

Fig. 7 Computed geometries of the exit transition states leading to **p8**, **p27**, and **p28**. Angles of the departing hydrogen atoms are given in degrees with respect to the rotation plane of the decomposing complex.

3.3.1. Products p8, p10, p40, p41, p41′ originating from CH radical addition to the C≡C bond and insertion into the C–H bond of dimethylacetylene (Fig. 3). The calculations reveal that the CH radical can add barrierlessly to the C≡C bond of dimethylacetylene and may insert into one of the C–H bonds of dimethylacetylene forming the three-member ring adducts **i80**, **i81**, and/or **i82**, and to acyclic intermediate **i83**, respectively. The collision complexes **i80**, **i81**, and **i82** are linked through low barriers of only 19 to 41 kJ mol^{-1} above **i80.** The decomposition of intermediate **i80** yields **p40** *via* atomic hydrogen emission from the cyclic C_3H moiety in **i80.** A hydrogen atom migration from the CH_3 group to the adjacent carbon atom in **i81** and/or **i82** forms intermediate **i84** and/or **i85**, respectively; the opening of the three-membered ring in intermediates **i81** and **i82** leads to acyclic intermediates **i86** and **i87**, respectively. The product **p41′** in singlet electronic state can be formed *via* atomic hydrogen emission from the CH moiety in **i87.** The ring opening of intermediate **i84** and/or **i85** results in the formation of intermediate **i90.** Hydrogen migrations from the CH_2 group in **i83** to the terminal CH_2 moiety and bare carbon atom lead to intermediates **i88** and **i89**, respectively. Intermediate **i88** can be formed *via* hydrogen migration from the CH group to the adjacent carbon atom in **i86** and **i87**. The decomposition of the intermediate **i88** leads to **p41** in the triplet state *via* atomic hydrogen emission from the CH moiety of **i88.** A hydrogen migration from the terminal CH_3

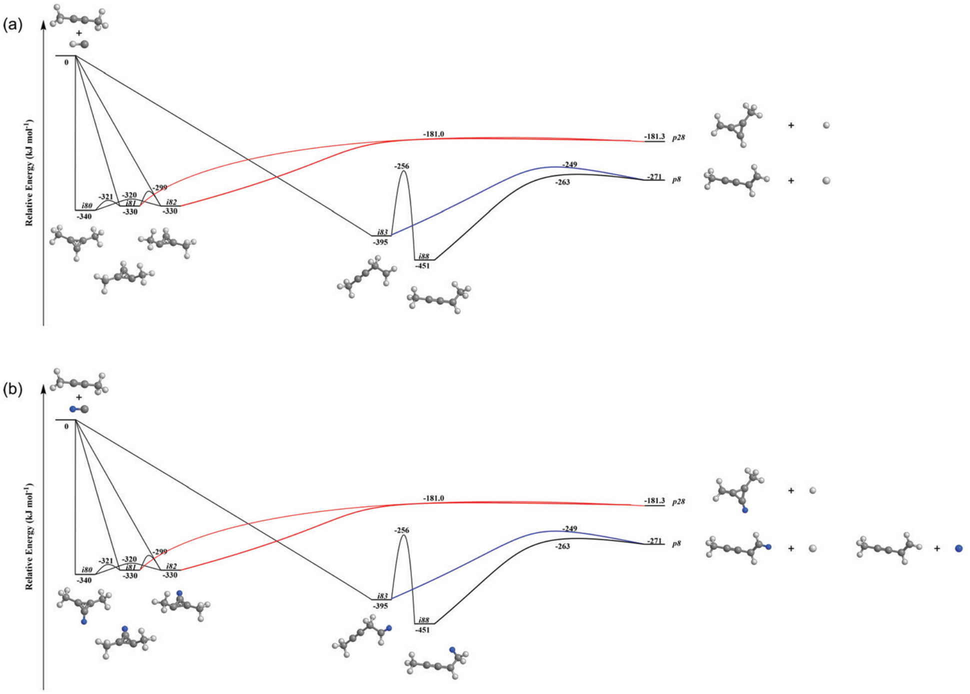

Fig. 8 Reduced PES of C_5H_7 (a) and C_5H_6D (b) leading to **p8** and **p28**. Energies are given for the fully hydrogenated reactant; energies of the (partially) deuterated species differ by a few kJ mol^{-1} at most. Atoms are colored as follows: carbon, black; hydrogen, grey; deuterium, blue.

Table 2 RRKM calculated product branching ratios (in %) for various initial complexes for the collision energies E_C of 0 and 20.6 kJ mol^{-1}

	Initial complexes							
	i80		**i81**		**i82**		**i83**	
Products	$E_C = 0$	$E_C = 20.6$	$E_C = 0$	$E_C = 20.6$	$E_C = 0$	$E_C = 20.6$	$E_C = 0$	$E_C = 20.6$
p2	0.00	0.00	0.00	0.00	0.00	0.00	0.20	0.20
p3	0.00	0.00	0.00	0.00	0.00	0.00	0.15	0.20
p8	0.02	0.00	0.02	0.00	0.02	0.00	91.94	90.10
p10	0.00	0.00	0.00	0.00	0.00	0.00	2.62	3.00
p23	0.01	0.00	0.01	0.00	0.01	0.00	1.96	2.10
p27	0.00	0.00	0.00	0.00	0.00	0.00	0.10	0.06
p28	97.37	96.50	97.39	96.60	97.39	96.60	0.00	0.00
p38	0.01	0.00	0.00	0.00	0.01	0.00	0.72	0.90
p39	1.54	2.00	1.54	2.00	1.54	2.00	0.00	0.00
p40	1.04	1.50	1.02	1.40	1.01	1.40	0.00	0.00
p42	0.00	0.00	0.00	0.00	0.00	0.00	2.25	3.40

moiety to the adjacent carbon atom in **i86** results in intermediates **i89** and **i91.** The intermediates **i89**, **i90**, **i91**, and **i92** are connected *via* low barriers of 23, 12, and 13 kJ mol^{-1} above **i89**, respectively. The hydrogen migration from the CH moiety to the adjacent carbon atom in **i89** and/or **i90** leads to **i15**; the latter can also be formed *via* the hydrogen migration from the terminal CH_3 group to the bare carbon atom of the CH_3C moiety in **i88.** The decomposition of intermediates **i83**, **i88**, **i89**, **i15**, and **i92** would lead to the product **p8** *via* atomic hydrogen loss from the nonterminal CH_2 group of **i83**, hydrogen atom emission from the CH_3 group in $CHCH_3$ moiety of **i88**, atomic hydrogen loss from the central CH group of **i89**, the hydrogen atom emission from CH moiety in **i15**, and the atomic hydrogen loss from central CH moiety in **i92.** Product **p10** can be formed *via* the hydrogen atom loss from CH moiety in **i15** and atomic hydrogen emission from the terminal CH_3C group of **i88.** It should be noted that in some cases, in particular, for **i80–p40**, **i82–i87**, **i87–p41′**, **i88–p41**, transition states could be located at the DFT ωB97X-D/6-311G(d,p) level of geometry optimization, but the further energy refinement at CCSD(T)-F12/cc-pVTZ-f12 brings their energies below those of the corresponding products. For H loss reaction steps, this result means that those occur without an exit barrier, *i.e.*, without a barrier in the reverse direction, whereas for **i82–i87**, the lower energy of the transition state compared to that of **i87** points at instability/metastability of this intermediate.

3.3.2. Products p1–p3, p12, p27, and p28 originating from CH radical addition to the C≡C bond and insertion into the C–H bond of dimethylacetylene (Fig. 5 and 6).

Fig. 4 illustrates

reaction pathways leading to products **p23** and **p38** of the loss of methyl and vinyl radicals, respectively. Since only the atomic hydrogen loss products could be observed in experiment, we do not discuss these pathways here. As seen in Fig. 5, the hydrogen migration from the CH_3 group to the nonadjacent bare carbon atom in **i86** and/or **i83** leads to **i32** and **i8**, respectively. Product **p2** can be formed *via* atomic hydrogen emission from the CH_3 group in **i32** *via* a rather loose transition state lying 9 kJ mol^{-1} above the energy of the separated products. The decomposition of intermediate **i8** yields **p3** *via* hydrogen atom loss from the nonterminal CH_2 moiety in **i8.** The hydrogen shift from the CH_3 group to the carbon atom in **i89** leads to **i4**; a hydrogen shift from the CH_2 group to the carbon atom in **i89** yields **i36.** The hydrogen atom migration from the CH_3 group to the carbon atom in **i90**, **i91**, and **i92** can form **i5**, **i4**, and **i3**, respectively. The conformers **i3**, **i4**, **i5** are linked *via* barriers of 43 kJ mol^{-1} above **i3.** The cyclic intermediate **i6** can be formed *via* ring closure of **i5.** The hydrogen shift from the CH moiety to the nonadjacent bare carbon atom and/or from terminal CH_3 group to the CH_2 group in **i92** leads to **i32.** Product **p1** can be formed *via* atomic hydrogen emission from the CH_2 group of **i6** *via* a loose transition state lying 11 kJ mol^{-1} above the separated products. The decomposition of intermediates **i4**, **i32**, and **i92** yield product **p2.** Product **p3** can be formed *via* hydrogen loss from the CH group of **i4**, from the nonterminal CH_2 group of **i8**, and from the CH_3 group of **i90** *via* loose transition states lying 10–16 kJ mol^{-1} above the separated products. The decomposition of intermediates **i81**, **i82**, **i84**, and **i85** yields **p28.** The ring closure of **i83** results in the intermediate **i96.** The product **p27** can be formed *via* hydrogen atom emission from the CH_3 group of **i96** *via* a loose transition state lying 11 kJ mol^{-1} above the separated products. The intermediate **i97** can be formed *via* ring closure of **i93**; the decomposition of **i97** yields the product **p12** *via* atomic hydrogen emission from the CH_2 group of **i97.**

Accounting for the results of our isotopic substitution experiments showing that the hydrogen atom emission originates from the dimethylacetylene reactant, we can exclude the formation of **p40**, **p41**′, and **i86** → **i91** → **i92** → **p8**; these pathways would require a hydrogen elimination from the methylidyne reactant or from both the methylidene and dimethylacetylene reactants (Fig. S2–S5, ESI†). For the initial adducts **i80**, **i81**, **i82**, and **i83**, considering significant barriers of over 180 kJ mol^{-1}, the hydrogen shifts between **i81** → **i84**, **i82** → **i85**, **i83** → **i8** are less competitive than the decomposition of intermediates **i81**, **i82**, **i83.** Further, compared to lower barriers of **i83** → **i88**, **i83** → **p8**, **i88** → **p8**, and isomerization of the key intermediates (**i89**, **i90**, **i91**, **i92**), the pathways **i83** → **i89**, **i88** → **p41**, **i88** → **p10**, **i89** → **i4**, **i90** → **i5**, **i90** → **p3**, **i91** → **i4**, **i92** → **i3**, **i92** → **i32**, and **i83** → **i89** would carry minor contribution. Therefore, the formation of products **p1**, **p2**, **p3**, **p12** can be ruled out. These findings suggest that **p8**, **p27**, and **p28** are likely products. Recall that the best fit center-of-mass angular distribution peaked at 90° (sideways scattering); this reveals that the dominating decomposition pathway of the C_5H_7 intermediate(s) involve(s) a hydrogen atom ejected perpendicularly to the rotational plane of the decomposing complex nearly parallel to the total angular momentum vector. The computed geometries of the exit transition states for **i81** → **p28**, **i82** → **p28**, **i88** → **p8**, and **i83** → **p8** can account for the sideways scattering (Fig. 7), but likely not **i96** → **p27**. Hence, **p8**, and **p28** are the most likely products as compiled in the reduced PES (Fig. 8). Furthermore, rather loose exit transition states for the decomposition pathways **i81** → **p28**, **i82** → **p28**, **i88** → **p8**, and **i83** → **p8** match our experimental data well. RRKM calculations predict in case of the CH radical addition to the C≡C bond of dimethylacetylene, **p28** along with atomic hydrogen to be the most likely product (97%), whereas **p39** (2%), and **p40** (1%) are minor products (Table 2). **p8** (90%) is the main product *via* CH radical insertion into the C–H bond of dimethylacetylene along with **p10** (3%), **p23** (2%), **p38** (1%), **p42** (3%) being minor products. It is interesting to note that the computed reaction energies for the formation of the dominating products formed *via* addition (**p28**, 97%) and insertion (**p8**, 90%) are −181 and −271 kJ mol^{-1}, respectively. These exoergicities do not correlate with our experimentally determined reaction energy of -56 ± 19 kJ mol^{-1}. This could mean that the reaction dynamics are non-statistical and a thermodynamically less stable product is formed or that the reaction are statistically leading to **p28** and/or **p8**, but a significant amount of available energy is channeled into internal excitation of the polyatomic reaction products. This would in turn lead to a shift of the maximum energy release to values significantly lower than in the limit of zero internal excitation. To discriminate between these two possibilities, quasiclassical trajectory (QCT) studies of the CH–CH_3CCCH_3 system are conducted.

3.4. Molecular dynamics simulations

Considering the aforementioned open questions, *ab initio* molecule dynamics (AIMD) simulations are employed to probe the dynamics of the reaction of the methylidyne radical with dimethylacetylene.[111] As discussed in Section 2.3, B3YLP/6-311G(d,p) theory is utilized for the AIMD simulations after carefully calibrating this level of theory with the benchmark potential energy profile. It is important to note that due to the excess energy, geometries observed in the trajectories are nearly all non-optimized structures deviating from those reported in the potential energy surface; however, for the conciseness of the manuscript, a trajectory is regarded as to have "visited" an intermediate over some period of time, if its geometries oscillate around the optimized structures of the intermediate. In this way, by labeling the sequence of the intermediates that a trajectory has visited over the whole course of the trajectory, the lifetime of the intermediates and reaction mechanism can be analyzed.

The products of the AIMD simulations of the bimolecular collision between dimethylacetylene and methylidyne radicals are summarized in Fig. 9(a). Since the number of trajectories at each impact parameter has been properly controlled as detailed in Section 2.3, the fraction reported in Fig. 9(a) can be interpreted as the product branching ratio. As observed in the experiments, the simulations reveal that the hydrogen loss products, including **p8**, **p28**, **p10**, and **p40** represent the

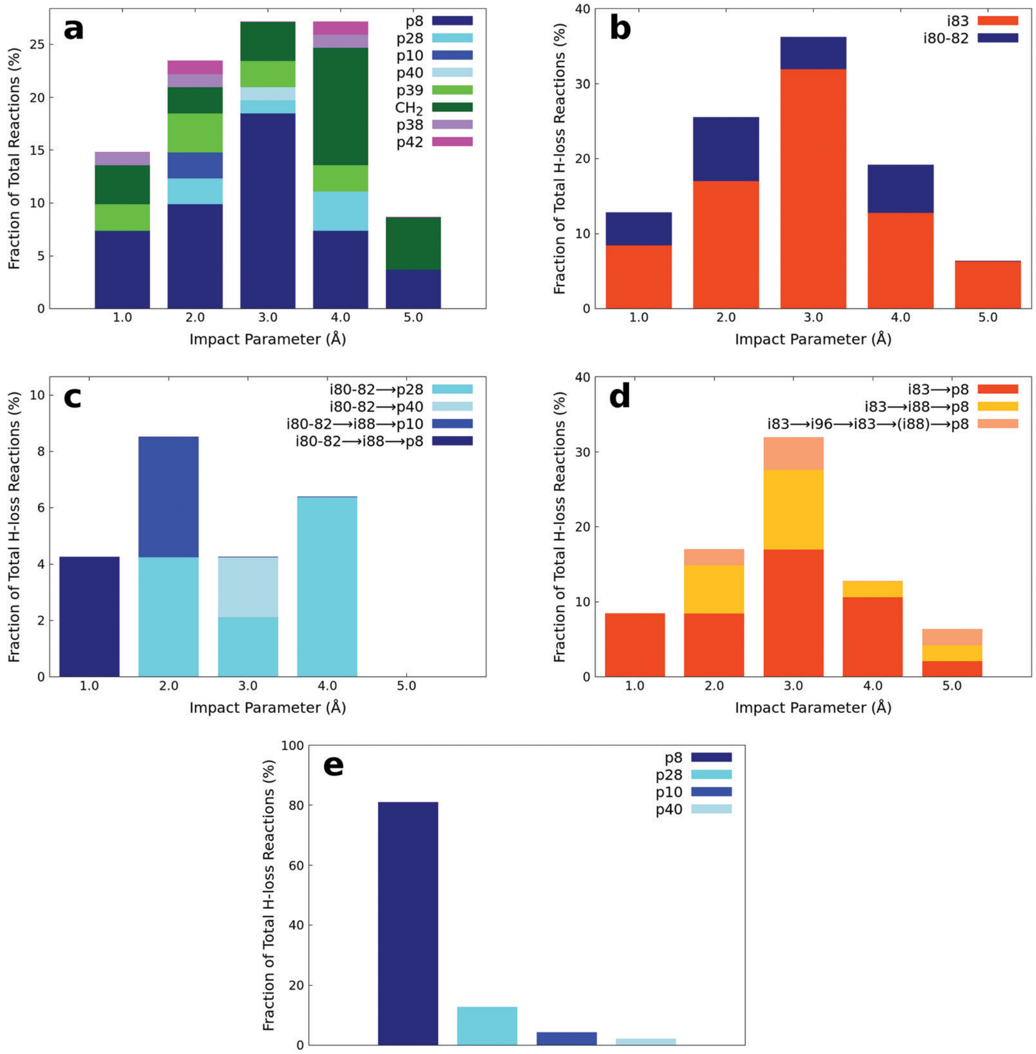

Fig. 9 (a) Fractions of products predicted to be formed from AIMD simulations at various impact parameters. Note that 'CH_2' (Fig. 9a) corresponds to the channel forming H_2CCCCH_3 plus CH_2. (b) The fraction of two entrance channels leading to **i80–i82** *vs.* **i83** trough addition *versus* insertion and eventually to **p28**, **p40**, **p10**, and **p8** at various impact parameters. (c) The fraction of different reaction pathways traversing through the **i80–i82** entrance channel at various impact parameters. (d) The fraction of different reaction pathways traversing through the **i83** entrance channel at various impact parameters. (e) The fraction of various hydrogen atom loss products integrated over all impact parameters.

majority of the products of this reaction. The analysis of the minor products is beyond the scope of this manuscript. The snapshots of representative AIMD trajectories can be found in Fig. 10. The AIMD simulations show that none of the hydrogen atom loss trajectories are direct; in other words, all of them involve indirect scattering dynamics *via* **i80–i82** through addition or **i83** through insertion-triggered hydrogen transfer before forming the products **p8**, **p28**, **p10**, and **p40**. Among these trajectories, the *overall* observed ratio between the **i80–i82** *vs.* **i83** entrance-channel complexes is about 1 : 4, *i.e.*, the dominance of insertion *versus* addition; its dependence on the impact parameter can be seen in Fig. 9(b). It is interesting to note that the amount of **i80–i82** in the entrance-channel is nearly independent on the impact parameter except for the largest value (5 Å), where the methylidyne is too far away from the center of the dimethylacetylene to trigger addition of methylidyne to the carbon–carbon triple bond. In contrast, the amount of **i83** in the entrance channel demonstrates a sharp peak at an impact parameter of 3 Å, which is nearly half of the length of dimethylacetylene, which facilitates the insertion of methylidyne into the methyl group.

The statistics of the trajectories traversing through **i80–i82** are illustrated in Fig. 9(c). About 60% of the trajectories form **p28** (**i80–82** → **p28**; SA1.mp4 (ESI†) for the animation of a representative trajectory) and 10% **p40** (**i80–82** → **p40**, SA2.mp4, ESI†). The remaining 30% of the trajectories isomerize to **i88** before dissociating to products **p10** (**i80–82** → **i88** → **p10**, SA3.mp4, ESI†) and **p8** (**i80–82** → **i88** → **p8**, SA4.mp4, ESI†) with a ratio of 1 : 1. These pathways reveal a strong impact parameter dependence. For example, the pathways involving **i88** are only observed at low impact parameters of 1 and 2 Å, while **p40** is only formed at large impact parameters of 3 Å.

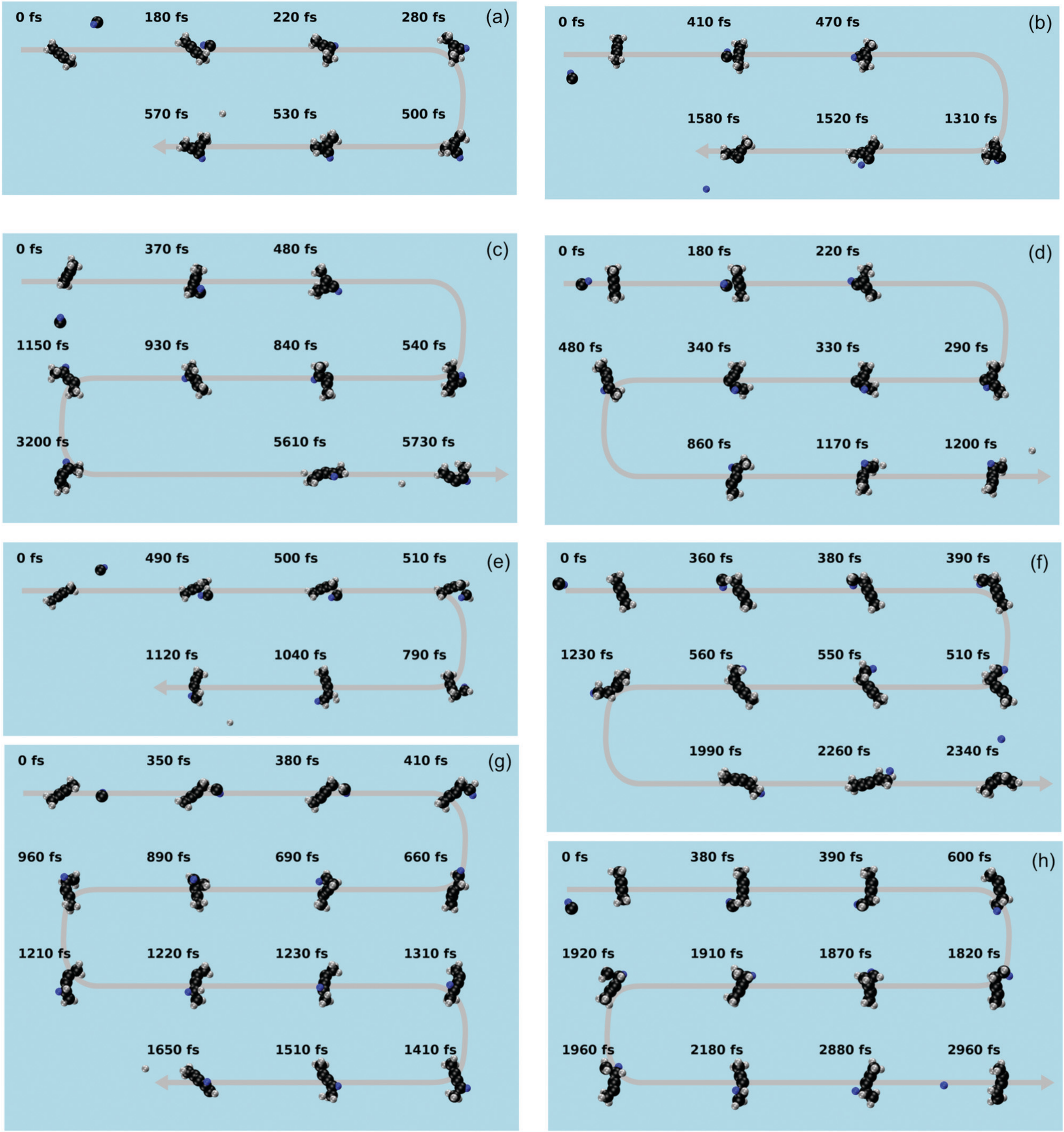

Fig. 10 Snapshots from a representative trajectory for each pathway. (a) **i80–i82** → **p28** (b) **i80–i82** → **p40** (c) **i80–i82** → **i88** → **p10** (d) **i80–i82** → **i88** → **p8** (e) **i83** → **p8** (f) **i83** → **i88** → **p8** (g) **i83** (↔**i96**) → **i88** → **p8** (h) **i83** (↔**i96**) → **p8**. The carbon and hydrogen atoms are portrayed as black and grey spheres, respectively. The hydrogen atom initially belonging to the methylidyne radical is colored in blue.

In contrast, among those trajectories passing through **i83**, only one product (**p8**) is observed. As Fig. 9(d) shows, about 61% of those trajectories lose a hydrogen atom and form **p8** (**i83** → **p8**, SA5.mp4, ESI†), about 28% isomerize to **i88** before forming **p8** (**i83** → **i88** → **p8**, SA6.mp4, ESI†), and the remaining fraction of 11% isomerizes back and forth *via* **i96** before forming **p8** with (**i83** (↔**i96**) → **i88** → **p8**, SA7.mp4, ESI†) or without (**i83** (↔**i96**) → **p8**, SA8.mp4, ESI†) eventually isomerizing to **i88**. The **i83** → **p8** pathway is the predominant pathway in almost all impact parameters except for the largest one. Comparing the **i83** entrance channel (Fig. 9(d)) to the **i80–82** entrance channel (Fig. 9(c)), it is interesting to note that **p8** can be formed in all impact parameter trajectories, in contrast to only the smallest (1 Å) in the latter.

It is essential to verify the validity of the results from dynamics simulations with experiments and RRKM calculations.

The branching ratio of the hydrogen loss products is depicted in Fig. 9(e). As shown, AIMD simulations report that the final hydrogen loss product distribution is predominantly **p8** (81.0%) followed by **p28** (12.7%) and trace amounts of **p10** (4.3%) and **p40** (2.0%). The product **p8** (100%) is the sole products through the **i83** entrance channel along with the dominant pathways **i83** → **p8** (∼61%) and **i83** → **i88** → **p8** (∼28%), whereas **p28** (∼60%), **p40** (∼10%), **p10** and **p8** (∼30%) are the products *via* the **i80–i82** entrance channel through pathways **i80–i82** → **p28** (∼60%). These findings match the experimental results derived from the comparison of the geometries of the exit transition states with the experimentally observed sideways scattering (**p8**, **p10**, and **p28**; Fig. 8) and RRKM calculations (Table 2), which predicts **p28** (99%) and **p40** (1%) in case of the methylidyne radical addition to the C≡C bond of dimethylacetylene; **p8** (97%) and **p10** (3%) *via* methylidyne radical insertion into the C–H bond of dimethylacetylene. The distribution of the relative translational energy of all four observed hydrogen atom loss products is summarized in Fig. 2. Although demonstrating a similar trend and matching the experimentally derived maximum translational energy, the AIMD simulations overestimate the most probable (AIMD: 40 ± 8 kJ mol^{-1}, exp: 12 ± 3 kJ mol^{-1}) relative translational energy of the products. Considering that our experimentally determined reaction energy of −56 ± 19 kJ mol^{-1} does not correlate with the computed reaction energies of the dominating products formed *via* addition (**p28**, −181 ± 4 kJ mol^{-1}) and insertion (**p8**, −271 ± 4 kJ mol^{-1}), the AIMD simulations verified that the reaction dynamics are statistical leading to **p28** and/or **p8**, but a significant amount of available energy is channeled into internal excitation of the polyatomic reaction products. Another factor is an artifact of AIMD; as stated in Section 2.3, AIMD simulation are halted when the products/reactants are formed, or the length of the trajectories has exceeded 8 ps due to the computation cost. As such, small portion of trajectories are stopped when still trapped in an intermediate. Due to the excess energy in the system, these trajectories will eventually dissociate given unlimited computing power, which would have be considered as long-lived, indirect trajectories that render products of low relative translational energy. Both factors result in a shift of the maximum energy release to values significantly lower than in the limit of zero internal excitation. In regard to the CM angular distribution, the AIMD simulations show "sideways scattering" (Fig. 2), which is in remarkable agreement with the experiments. These CM functions (Fig. 2) derived from the dynamics simulations fail to fit the TOF data and the laboratory angular distribution well (Fig. 1); this is predominantly due to the distribution maximum in the center-of-mass translational energy distribution, which is shifted to higher energies compared to the experimental data. This in turn leads to simulated TOFs which are too fast and also to a simulated LAB distribution which is too broad compared to the experimental findings. Further, the individual CM functions of each dominant product channels to **p8** and **p28** are also compared with the experimental results (Fig. S6–S10, ESI†). Considering the center-of-mass translational energy distributions, a similar maximum translational energy of **p8** is revealed in AIMD simulations (98 kJ mol^{-1}) and in the experimental results (77 ± 19 kJ mol^{-1}) (Fig. S7, ESI†). However, the AIMD simulations predict the most probable relative translational energy of **p8** to be 41 ± 8 kJ mol^{-1} compared with experimental results of 12 ± 3 kJ mol^{-1}. Both AIMD simulations and experimental results featured with "sideway scattering" of CM angular distribution $T(\theta)$ of **p8** (Fig. S7, ESI†). The CM functions of **p8** (Fig. S7, ESI†) from the AIMD simulations fit the TOF data and the laboratory angular distribution well (Fig. S6, ESI†). For the formation of **p28**, the AIMD simulations reveal the relative translational energy distribution $P(E_T)$ of **p28** terminated at about 65 kJ mol^{-1} which is in good agreement with 77 ± 19 kJ mol^{-1} from the experiments (Fig. S9, ESI†). The distribution maximum of $P(E_T)$ of **p28** in AIMD simulations is 33 ± 16 kJ mol^{-1}, once again higher than the experimental value of 12 ± 3 kJ mol^{-1} (Fig. S9, ESI†). The CM angular distribution $T(\theta)$ of **p28** (Fig. S9, ESI†) derived in the AIMD simulations and experimental results are both characterized as "sideway scattering", but AIMD simulations also carries a slightly backward scattering. The difference of the CM functions between AIMD simulations and the experimental results leads to the deviation to fit the TOF data and the laboratory angular distribution (Fig. S8, ESI†).

Table 3 The percentage of the products of the hydrogen atom loss in the trajectories leading to **p8/28/10/40** (Fig. 3 and 6) with the hydrogen atom initially belonging to the methylidyne (CH) reactant. "—" denotes that the products are not found at all, while "0" denotes that the products are found, but none of the product hydrogen atom initially belongs to the CH

	Impact parameter (A)					
Products	1.0	2.0	3.0	4.0	5.0	Overall (%)
H-loss	0	8.3	17.6	0	33.3	10.6
p8	0	12.5	13.3	0	33.3	10.5
p28	—	0	0	0	—	0
p10	—	0	—	—	—	0
p40	—	—	100	—	—	100

Finally, the origin of the hydrogen atom – either from dimethylacetylene or methylidyne reactant – in the atomic hydrogen loss pathways is also analyzed; the results are summarized in Table 3. As shown, AIMD trajectories show that over 90% of the hydrogen atom in the hydrogen atom loss pathways originates from the methyl groups of the dimethylacetylene reactant, which is in agreement with the experiment exploiting D1-methylidyne radical reactants.

4. Conclusion

Our crossed molecular beam experiment of the methylidyne (CH; $X^2\Pi$) radical with dimethylacetylene (CH_3CCCH_3; X^1A_{1g}) reveals that the reaction proceeds barrierlessly *via* indirect scattering dynamics through long-lived C_5H_7 reaction intermediate(s) ultimately dissociating to C_5H_6 isomers along with atomic hydrogen. Experiments were also conducted by replacing the CH with CD; these studies revealed that in the methylidyne–dimethylacetylene reaction, the hydrogen atom is lost predominantly from the methyl groups of the dimethylacetylene reactant. The center of mass functions suggest an overall reaction energy of −56 ± 19 kJ mol^{-1} with the CM angular distribution $T(\theta)$ depicting a "sideway scattering" and hence a hydrogen atom loss predominantly parallel to the total angular momentum vector. *Ab initio* electronic structure and statistical Rice–Ramsperger–Kassel–Marcus (RRKM) calculations suggest that 1-penten-3-yne (**p8**) and 1-methyl-3-methylenecyclopropene (**p28**) are the most likely atomic hydrogen loss products. The reaction has no entrance barrier; all barriers involved in the formation of 1-penten-3-yne (**p8**) and 1-methyl-3-methylenecyclopropene (**p28**) are well below the energy of the separated reactants, and the overall reactions to prepare both isomers are exoergic by -181 ± 4 kJ mol^{-1} (**p28**) and -271 ± 4 kJ mol^{-1} (**p8**), respectively. These energetics do not match the experimentally derived reaction energy of -56 ± 19 kJ mol^{-1}, suggesting that the reaction is either non-statistical or that a significant amount of the energy is channeled into the internal rovibrational modes of the heavy products. To untangle the actual reaction pathways, AIMD simulations were carried out. The latter verified that the reaction dynamics are statistical leading predominantly to **p28** (13%) and **p8** (81%), but a significant amount of available energy is channeled into the internal excitation of the polyatomic reaction products. The dynamics are controlled by addition to the carbon–carbon triple bond with the reaction intermediates **i80**, **i81**, and **i82** eventually eliminating a hydrogen atom from the methyl groups of the dimethylacetylene reactant forming 1-methyl-3-methylenecyclopropene **p28** (13%). The dominating pathways reveal an unexpected insertion of methylidyne into one of the six carbon-hydrogen single bonds of the methyl groups of dimethylacetylene leading to the acyclic intermediate **i83**; intermediate **i88** is formed *via* hydrogen atom shift in **i83**; the decomposition of **i83** and **i88** lead to 1-penten-3-yne (**p8**, -271 ± 4 kJ mol^{-1}) – also called 1-vinylmethylacetylene – with relative fractions of **p8** formation of 66% from **i83** and 34% from **i88**. Since the involvement of **i88** is expected in the release of atomic hydrogen and atomic deuterium (Fig. 8), the low percentage of **i88** in the formation of **p8** is also supported by the experimental findings of the D1-methylidyne–dimethylacetylene reaction. Therefore, the methyl groups of dimethylacetylene effectively 'screen' the carbon–carbon triple bond from being attacked by addition (**i80**, **i81**, **i82**) thus directing the dynamics to an insertion process forming **i83**. The AIMD simulations suggest that the overall ratio in the entrance channel of insertion (**i80–i82**) *vs.* addition (**i83**) is 1 : 4, while the ratio between the final hydrogen loss products **p8** *vs.* **p28** is about 6 : 1. These findings propose that the combination of the crossed molecular beam experiments with electronic structure calculations and quasiclassical trajectory (QCT) studies provide persuasive evidence on the formation of 1-penten-3-yne (**p8**) and 1-methyl-3-methylenecyclopropene (**p28**) under single collision conditions *via* the bimolecular reaction of the methylidyne radical with dimethylacetylene in the gas phase involving indirect scattering dynamics.

Conflicts of interest

There are no conflicts to declare.

Acknowledgements

This work was supported by the U.S. Department of Energy, Basic Energy Sciences DE-FG02-03ER15411 and DE-FG02-04ER15570 to the University of Hawaii and to Florida International University, respectively. *Ab initio* calculations at Lebedev Physics Institute were supported by the Ministry of Science and Higher Education of the Russian Federation under Grant No. 075-15-2021-597.

References

1 C. E. Otis, J. L. Knee and P. M. Johnson, *J. Chem. Phys.*, 1983, **78**, 2091–2092.
2 N. Nakashima and K. Yoshihara, *J. Chem. Phys.*, 1982, **77**, 6040–6050.
3 H. R. Ward and J. S. Wishnok, *J. Am. Chem. Soc.*, 1968, **90**, 5353–5357.
4 J. P. Reilly and K. L. Kompa, *J. Chem. Phys.*, 1980, **73**, 5468–5476.
5 W. Radloff, T. Freudenberg, H.-H. Ritze, V. Stert, F. Noack and I. V. Hertel, *Chem. Phys. Lett.*, 1996, **261**, 301–306.
6 J. Park, R. Bersohn and I. Oref, *J. Chem. Phys.*, 1990, **93**, 5700–5708.
7 J. K. Foote, M. H. Mallon and J. N. Pitts Jr, *J. Am. Chem. Soc.*, 1966, **88**, 3698–3702.
8 H. R. Ward and P. D. Sherman, *J. Am. Chem. Soc.*, 1967, **89**, 1962–1963.
9 L. Kaplan and K. E. Wilzbach, *J. Am. Chem. Soc.*, 1967, **89**, 1030–1031.
10 L. Kaplan, S. P. Walch and K. E. Wilzbach, *J. Am. Chem. Soc.*, 1968, **90**, 5646–5647.
11 F. Mellows and S. Lipsky, *J. Phys. Chem.*, 1966, **70**, 4076–4077.
12 A. Yokoyama, X. Zhao, E. J. Hintsa, R. E. Continetti and Y. T. Lee, *J. Chem. Phys.*, 1990, **92**, 4222–4233.
13 L. K. Madden, A. M. Mebel, M.-C. Lin and C. F. Melius, *J. Phys. Org. Chem.*, 1996, **9**, 801–810.
14 A. M. Mebel, M.-C. Lin, T. Yu and K. Morokuma, *J. Phys. Chem. A*, 1997, **101**, 3189–3196.
15 H. Wiesemeyer, R. Güsten, K. M. Menten, C. A. Durán, T. Csengeri, A. M. Jacob, R. Simon, J. Stutzki and F. Wyrowski, *Astron. Astrophys.*, 2018, **612**, A37.
16 M. Gerin, M. De Luca, J. R. Goicoechea, E. Herbst, E. Falgarone, B. Godard, T. A. Bell, A. Coutens, M. Kazmierczak, P. Sonnentrucker, J. H. Black, D. A. Neufeld, T. G. Phillips, J. Pearson, P. B. Rimmer, G. Hassel, D. C. Lis, C. Vastel, F. Boulanger, J. Cernicharo, E. Dartois, P. Encrenaz, T. Giesen, P. F. Goldsmith, H. Gupta, C. Gry, P. Hennebelle, P. Hily-Blant, C. Joblin, R. Koos, J. Kreowski, J. Matrín-Pintado, R. Monje, B. Mookerjea, M. Perault, C. Persson, R. Plume, M. Salez, M. Schmidt, J. Stutzki, D. Teyssier, S. Yu, A. Contursi, K. Menten, T. R. Geballe, S. Schlemmer, P. Morris, W. A. Hatch, M. Imram, J. S. Ward, E. Caux, R. Güsten, T. Klein, P. Roelfsema, P. Dieleman,

R. Schieder, N. Honingh and J. Zmuidzinas, *Astron. Astrophys.*, 2010, **521**, L16.
17 A. C. Danks, S. R. Federman and D. L. Lambert, *Astron. Astrophys.*, 1984, **130**, 62–66.
18 B. H. Andrew, L. W. Avery and N. W. Broten, *Astron. Astrophys.*, 1978, **66**, 437–439.
19 M. Sumitani, D. V. O'Connor, Y. Takagi, N. Nakashima, K. Kamogawa, Y. Udagawa and K. Yoshihara, *Chem. Phys.*, 1985, **93**, 359–371.
20 K. Shindo and S. Lipsky, *J. Chem. Phys.*, 1966, **45**, 2292–2297.
21 S.-T. Tsai, C.-K. Lin, Y. T. Lee and C.-K. Ni, *J. Chem. Phys.*, 2000, **113**, 67–70.
22 R. I. Kaiser, P. Maksyutenko, C. Ennis, F. Zhang, X. Gu, S. P. Krishtal, A. M. Mebel, O. Kostko and M. Ahmed, *Faraday Discuss.*, 2010, **147**, 429–478.
23 R. I. Kaiser and N. Hansen, *J. Phys. Chem. A*, 2021, **125**, 3826–3840.
24 M. A. Duncan, T. G. Dietz, M. G. Liverman and R. E. Smalley, *J. Phys. Chem.*, 1981, **85**, 7–9.
25 S.-T. Tsai, C.-L. Huang, Y. T. Lee and C.-K. Ni, *J. Chem. Phys.*, 2001, **115**, 2449–2455.
26 T. C. Hsu, J. Shu, Y. Chen, J. J. Lin, Y. T. Lee and X. Yang, *J. Chem. Phys.*, 2001, **115**, 9623–9626.
27 T. C. Hsu, J. Shu, Y. Chen, J. J. Lin, Y. T. Lee and X. Yang, *J. Chin. Chem. Soc.*, 2002, **49**, 1–6.
28 D. Xu and D. Li, *Astrophys. J.*, 2016, **833**, 90.
29 K. Sellgren, R. G. Smith and T. Y. Brooke, *Astrophys. J.*, 1994, **433**, 179–186.
30 B. Larsson and R. Liseau, *Astron. Astrophys.*, 2017, **608**, A133.
31 Y. C. Minh, H. B. Liu and R. Galvań-Madrid, *Astrophys. J.*, 2016, **824**, 99.
32 O. Kochina and D. Wiebe, *Origins Life Evol. Biosphere*, 2014, **44**, 169–174.
33 J. L. Neill, E. A. Bergin, D. C. Lis, P. Schilke, N. R. Crockett, C. Favre, M. Emprechtinger, C. Comito, S.-L. Qin, D. E. Anderson, A. M. Burkhardt, C. Jo-Hsin, B. J. Harris, S. D. Lord, B. A. McGuire, T. D. McNeill, R. R. Monje, T. G. Phillips, A. L. Steber, T. Vasyunina and S. Yu, *Astrophys. J.*, 2014, **789**, 8.
34 B. Gans, S. Boyé-Péronne, M. Broquier, M. Delsaut, S. Douin, C. E. Fellows, P. Halvick, J.-C. Loison, R. R. Lucchese and D. Gauyacq, *Phys. Chem. Chem. Phys.*, 2011, **13**, 8140–8152.
35 Z. Peng, M. Dobrijevic, E. Hébrard, N. Carrasco and P. Pernot, *Faraday Discuss.*, 2010, **147**, 137–153.
36 M. Dobrijevic, J. C. Loison, K. M. Hickson and G. Gronoff, *Icarus*, 2016, **268**, 313–339.
37 J. M. Ribeiro and A. M. Mebel, *Mol. Phys.*, 2015, **113**, 1865–1872.
38 M. Dobrijevic, E. Hébrard, J. C. Loison and K. M. Hickson, *Icarus*, 2014, **228**, 324–346.
39 P. Lavvas, M. Galand, R. V. Yelle, A. N. Heays, B. R. Lewis, G. R. Lewis and A. J. Coates, *Icarus*, 2011, **213**, 233–251.
40 A. Faure, V. Vuitton, R. Thissen and L. Wiesenfeld, *J. Phys. Chem. A*, 2009, **113**, 13694–13699.
41 E. Hébrard, M. Dobrijevic, P. Pernot, N. Carrasco, A. Bergeat, K. M. Hickson, A. Canosa, S. D. Le Picard and I. R. Sims, *J. Phys. Chem. A*, 2009, **113**, 11227–11237.
42 A. Canosa, I. R. Sims, D. Travers, I. W. M. Smith and B. R. Rowe, *Astron. Astrophys.*, 1997, **323**, 644–651.
43 X. Zhang, J. M. Ajello and Y. L. Yung, *Astrophys. J. Lett.*, 2009, **708**, L18–L21.
44 M. R. Berman and M.-C. Lin, *Chem. Phys.*, 1983, **82**, 435–442.
45 M. R. Berman, J. W. Fleming, A. B. Harvey and M.-C. Lin, *Chem. Phys.*, 1982, **73**, 27–33.
46 A. Merkel, I. Borger, H. J. Spangenberg and L. Zuelicke, *Z. Phys. Chem.*, 1982, **263**, 449–460.
47 J. E. Butler, J. W. Fleming, L. P. Goss and M.-C. Lin, *Chem. Phys.*, 1981, **56**, 355–365.
48 W. Boullart, K. Devriendt, R. Borms and J. Peeters, *J. Phys. Chem.*, 1996, **100**, 998–1007.
49 A. M. Mebel, in *Reviews of Modern Quantum Chemistry*, ed. G. Maroulis and K. D. Sen, World Scientific, Singapore, 2002, p. 340.
50 H. F. Bettinger, P. R. Schreiner, H. F. Schaefer and P. V. R. Schleyer, *J. Am. Chem. Soc.*, 1998, **120**, 5741–5750.
51 J.-C. Loison and A. Bergeat, *Phys. Chem. Chem. Phys.*, 2009, **11**, 655–664.
52 A. M. Mebel, M.-C. Lin, D. Chakraborty, J. Park, S. H. Lin and Y. T. Lee, *J. Chem. Phys.*, 2001, **114**, 8421–8435.
53 J. A. Miller and C. F. Melius, *Combust. Flame*, 1992, **91**, 21–39.
54 N. Daugey, P. Caubet, B. Retail, M. Costes, A. Bergeat and G. Dorthe, *Phys. Chem. Chem. Phys.*, 2005, **7**, 2921–2927.
55 C. F. Melius, J. A. Miller and E. M. Evleth, *Symp. (Int.) Combust.*, 1992, **24**, 621–628.
56 R. I. Kaiser, D. S. N. Parker and A. M. Mebel, *Annu. Rev. Phys. Chem.*, 2015, **66**, 43–67.
57 D. S. N. Parker, A. M. Mebel and R. I. Kaiser, *Chem. Soc. Rev.*, 2014, **43**, 2701–2713.
58 R. I. Kaiser and A. M. Mebel, *Chem. Soc. Rev.*, 2012, **41**, 5490–5501.
59 N. Balucani, F. Zhang and R. I. Kaiser, *Chem. Rev.*, 2010, **110**, 5107–5127.
60 X. Gu and R. I. Kaiser, *Acc. Chem. Res.*, 2009, **42**, 290–302.
61 X. Gu, R. I. Kaiser and A. M. Mebel, *ChemPhysChem*, 2008, **9**, 350–369.
62 R. I. Kaiser and A. M. Mebel, *Int. Rev. Phys. Chem.*, 2002, **21**, 307–356.
63 R. I. Kaiser, *Chem. Rev.*, 2002, **102**, 1309–1358.
64 D. S. N. Parker and R. I. Kaiser, *Chem. Soc. Rev.*, 2017, **46**, 452–463.
65 N. Balucani, *Chem. Soc. Rev.*, 2012, **41**, 5473–5483.
66 N. Balucani, *Int. J. Mol. Sci.*, 2009, **10**, 2304–2335.
67 N. Balucani, G. Capozza, F. Leonori, E. Segoloni and P. Casavecchia, *Int. Rev. Phys. Chem.*, 2006, **25**, 109–163.
68 P. Casavecchia, N. Balucani and G. G. Volpi, *Annu. Rev. Phys. Chem.*, 1999, **50**, 347–376.
69 P. Casavecchia, N. Balucani, M. Alagia, L. Cartechini and G. G. Volpi, *Acc. Chem. Res.*, 1999, **32**, 503–511.

70 C. He, A. A. Nikolayev, L. Zhao, A. M. Thomas, S. Doddipatla, G. R. Galimova, V. N. Azyazov, A. M. Mebel and R. I. Kaiser, *J. Phys. Chem. A*, 2021, **125**, 126–138.

71 C. He, L. Zhao, S. Doddipatla, A. M. Thomas, A. A. Nikolayev, G. R. Galimova, V. N. Azyazov, A. M. Mebel and R. I. Kaiser, *ChemPhysChem*, 2020, **21**, 1295–1309.

72 C. He, A. M. Thomas, G. R. Galimova, A. M. Mebel and R. I. Kaiser, *J. Phys. Chem. A*, 2019, **123**, 10543–10555.

73 C. He, A. M. Thomas, G. R. Galimova, A. N. Morozov, A. M. Mebel and R. I. Kaiser, *J. Am. Chem. Soc.*, 2020, **142**, 3205–3213.

74 C. He, G. R. Galimova, Y. Luo, L. Zhao, A. K. Eckhardt, R. Sun, A. M. Mebel and R. I. Kaiser, *Proc. Natl. Acad. Sci. U. S. A.*, 2020, **117**, 30142–30150.

75 S. Doddipatla, G. R. Galimova, H. Wei, A. M. Thomas, C. He, Z. Yang, A. N. Morozov, C. N. Shingledecker, A. M. Mebel and R. I. Kaiser, *Sci. Adv.*, 2021, **7**, eabd4044.

76 A. M. Thomas, L. Zhao, C. He, G. R. Galimova, A. M. Mebel and R. I. Kaiser, *Angew. Chem., Int. Ed.*, 2019, **58**, 15488–15495.

77 R. I. Kaiser, X. Gu, F. Zhang and P. Maksyutenko, *Phys. Chem. Chem. Phys.*, 2012, **14**, 575–588.

78 P. Maksyutenko, F. Zhang, X. Gu and R. I. Kaiser, *Phys. Chem. Chem. Phys.*, 2011, **13**, 240–252.

79 F. Zhang, P. Maksyutenko and R. I. Kaiser, *Phys. Chem. Chem. Phys.*, 2012, **14**, 529–537.

80 G. O. Brink, *Rev. Sci. Instrum.*, 1966, **37**, 857–860.

81 N. R. Daly, *Rev. Sci. Instrum.*, 1960, **31**, 264–267.

82 P. S. Weiss, *Reaction Dynamics of Electronically Excited Alkali Atoms with Simple Molecules*, PhD thesis, University of California at Berkeley, Berkeley, CA, 1986.

83 M. F. Vernon, *Molecular Beam Scattering*, PhD thesis, University of California at Berkeley, Berkeley, CA, 1983.

84 R. I. Kaiser, Y. T. Lee and A. G. Suits, *J. Chem. Phys.*, 1996, **105**, 8705–8720.

85 R. I. Kaiser, D. Stranges, Y. T. Lee and A. G. Suits, *J. Chem. Phys.*, 1996, **105**, 8721–8733.

86 R. I. Kaiser, C. Ochsenfeld, D. Stranges, M. Head-Gordon and Y. T. Lee, *Faraday Discuss.*, 1998, **109**, 183–204.

87 X. Gu, Y. Guo, F. Zhang, A. M. Mebel and R. I. Kaiser, *Faraday Discuss.*, 2006, **133**, 245–275.

88 A. M. Mebel and R. I. Kaiser, *Int. Rev. Phys. Chem.*, 2015, **34**, 461–514.

89 J.-D. Chai and M. Head-Gordon, *Phys. Chem. Chem. Phys.*, 2008, **10**, 6615–6620.

90 G. Knizia, T. B. Adler and H.-J. Werner, *J. Chem. Phys.*, 2009, **130**, 054104.

91 T. B. Adler, G. Knizia and H.-J. Werner, *J. Chem. Phys.*, 2007, **127**, 221106.

92 T. H. Dunning Jr, *J. Chem. Phys.*, 1989, **90**, 1007–1023.

93 J. Zhang and E. F. Valeev, *J. Chem. Theory Comput.*, 2012, **8**, 3175–3186.

94 M. J. Frisch, G. W. Trucks, H. B. Schlegel, G. E. Scuseria, M. A. Robb, J. R. Cheeseman, G. Scalmani, V. Barone, B. Mennucci, G. A. Petersson, H. Nakatsuji, M. Caricato, X. Li, H. P. Hratchian, A. F. Izmaylov, J. Bloino, G. Zheng, J. L. Sonnenberg, M. Hada, M. Ehara, K. Toyota, R. Fukuda, J. Hasegawa, M. Ishida, T. Nakajima, Y. Honda, O. Kitao, H. Nakai, T. Vreven, J. A. Montgomery, Jr., J. E. Peralta, F. Ogliaro, M. Bearpark, J. J. Heyd, E. Brothers, K. N. Kudin, V. N. Staroverov, R. Kobayashi, J. Normand, K. Raghavachari, A. Rendell, J. C. Burant, S. S. Iyengar, J. Tomasi, M. Cossi, N. Rega, J. M. Millam, M. Klene, J. E. Knox, J. B. Cross, V. Bakken, C. Adamo, J. Jaramillo, R. Gomperts, R. E. Stratmann, O. Yazyev, A. J. Austin, R. Cammi, C. Pomelli, J. W. Ochterski, R. L. Martin, K. Morokuma, V. G. Zakrzewski, G. A. Voth, P. Salvador, J. J. Dannenberg, S. Dapprich, A. D. Daniels, Ö. Farkas, J. B. Foresman, J. V. Ortiz, J. Cioslowski and D. J. Fox, *Gaussian 09, Revision A. 1, Gaussian*, Gaussian Inc., Wallingford, CT, 2009, vol. 200, p. 28.

95 H.-J. Werner, P. J. Knowles, R. Lindh, F. R. Manby, M. Schütz, P. Celani, T. Korona, G. Rauhut, R. D. Amos and A. Bernhardsson, *MOLPRO, Version 2010.1, A Package of Ab Initio Programs*, University of Cardiff, Cardiff, UK, 2010.

96 P. J. Robinson and K. A. Holbrook, *Unimolecular Reactions*, Wiley, New York, 1972.

97 H. Eyring, S. H. Lin and S. M. Lin, *Basic Chemical Kinetics*, John Wiley and Sons, Inc., New York, 1980.

98 J. I. Steinfeld, J. S. Francisco and W. L. Hase, *Chemical Kinetics and Dynamics*, Prentice Hall Englewood Cliffs (New Jersey), 1982.

99 C. He, L. Zhao, A. M. Thomas, A. N. Morozov, A. M. Mebel and R. I. Kaiser, *J. Phys. Chem. A*, 2019, **123**, 5446–5462.

100 V. V. Kislov, T. L. Nguyen, A. M. Mebel, S. H. Lin and S. C. Smith, *J. Chem. Phys.*, 2004, **120**, 7008–7017.

101 C. Møller and M. S. Plesset, *Phys. Rev.*, 1934, **46**, 618.

102 A. D. Becke, *J. Chem. Phys.*, 1993, **98**, 1372–1377.

103 A. D. Becke, *J. Chem. Phys.*, 1997, **107**, 8554–8560.

104 H. L. Schmider and A. D. Becke, *J. Chem. Phys.*, 1998, **108**, 9624–9631.

105 Y. Zhao and D. G. Truhlar, *J. Phys. Chem. A*, 2004, **108**, 6908–6918.

106 Y. Zhao and D. G. Truhlar, *J. Phys. Chem. A*, 2006, **110**, 13126–13130.

107 C. Adamo and V. Barone, *J. Chem. Phys.*, 1999, **110**, 6158–6170.

108 R. Krishnan, J. S. Binkley, R. Seeger and J. A. Pople, *J. Chem. Phys.*, 1980, **72**, 650–654.

109 S. Doddipatla, C. He, R. I. Kaiser, Y. Luo, R. Sun, G. R. Galimova, A. M. Mebel and T. J. Millar, *Proc. Natl. Acad. Sci. U. S. A.*, 2020, **117**, 22712–22719.

110 Y. Luo, K. Fujioka, A. Shoji, W. L. Hase, K.-M. Weitzel and R. Sun, *J. Phys. Chem. A*, 2020, **124**, 9119–9127.

111 S. Pratihar, X. Ma, Z. Homayoon, G. L. Barnes and W. L. Hase, *J. Am. Chem. Soc.*, 2017, **139**, 3570–3590.

112 W. L. Hase, R. J. Duchovic, X. Hu, A. Komornicki, K. F. Lim, D.-H. Lu, G. H. Peslherbe, K. N. Swamy, S. R. V. Linde, A. Varandas, H. Wang and R. J. Wolf, *QCPE*, 1996, **16**, 671.

113 X. Hu, W. L. Hase and T. Pirraglia, *J. Comput. Chem.*, 1991, **12**, 1014–1024.

114 M. Valiev, E. J. Bylaska, N. Govind, K. Kowalski, T. P. Straatsma, H. J. J. Van Dam, D. Wang, J. Nieplocha, E. Apra, T. L. Windus and W. A. de Jong, *Comput. Phys. Commun.*, 2010, **181**, 1477–1489.

115 U. Lourderaj, R. Sun, S. C. Kohale, G. L. Barnes, W. A. de Jong, T. L. Windus and W. L. Hase, *Comput. Phys. Commun.*, 2014, **185**, 1074–1080.

116 R. D. Levine, R. B. Bernstein and Y. T. Lee, *Phys. Today*, 1988, **41**, 90–92.

117 R. D. Levine, *Molecular Reaction Dynamics*, Cambridge University Press, Cambridge, 2005.

118 D. R. Herschbach, *Discuss. Faraday Soc.*, 1962, **33**, 149–161.

119 W. B. Miller, S. A. Safron and D. R. Herschbach, *Discuss. Faraday Soc.*, 1967, **44**, 108–122.